An Analytical Solution of Radiative Transfer in the Coupled Atmosphere-Ocean System with Rough Surface

Zhonghai Jin
AS&M, Inc.
One Enterprise PKWY, STE 300
Hampton, VA 23666

Thomas P. Charlock
Mail Stop 420
Division of Atmospheric Sciences
NASA Langley Research Center
Hampton, Virginia 23681-2199

Ken Rutledge
AS&M, Inc.
One Enterprise PKWY, STE 300
Hampton, VA 23666

Knut Stamnes
Department of Physics & Engineering Physics
Stevens Institute of Technology
Hoboken, NJ 07030

Yingjian Wang
Anhui Institute of Optics and Fine Mechanics
Chinese Academy of Sciences
Hefei, Anhui 230031, China

Abstract

Using the computationally efficient discrete-ordinate method, we present an analytical solution for radiative transfer in the coupled atmosphere-ocean system with rough air-water interface. The theoretical formulations of the radiative transfer equation and solution are described. The effects of surface roughness on the radiation field in the atmosphere and ocean are studied and compared with satellite and surface measurements. The results show that ocean surface roughness has significant effects on the upwelling radiation in the atmosphere and the downwelling radiation in the ocean. As wind speed increases, the angular domain of sunglint broadens, the surface albedo decreases, and the transmission to the ocean increases. The downward radiance field in the upper ocean is highly anisotropic, but this anisotropy decreases rapidly as surface wind increases and as depth in ocean increases. The effects of surface roughness on radiation also depend greatly on both wavelength and angle of incidence (i.e., solar elevation); these effects are significantly smaller throughout the spectrum at high sun. The model-observation discrepancies may indicate that the Cox-Munk surface roughness model is not sufficient for high wind conditions.

1. Introduction

Cox and Munk[1] described the statistical charactersitics of reflection by wind-blown ocean waves by modeling the sea surface as a collection of individual mirror facets. They presented the probability distribution for the slopes of surface facets as a wind-speed dependent Guassian function. Based on this Cox and Munk formulation, several researchers incorporated the ocean surface roughness in their radiative transfer models[2-8]. Most of these models used the ray tracing method or the Monte Carlo technique to treat the surface roughness. The Monte Carlo approach consists of using probabilistic concepts and has the advantage for geometries other than the plane-parallel. Implementation of the statistical surface roughness by the Monte Carlo method is relatively straightforward. The discrete-ordinate technique, on the other hand, can be more computationally efficient and accurate, because it solves the radiative transfer equation analytically without the enormous statistical sample required to close a Monte Carlo solution and without the statistical fluctuation error. However, due to its analytical nature, implementation of the surface roughness in a discrete-ordinate radiative transfer code is more complicated; a rigorous solution involves an additional parameter that results in a different analytical solution from the flat surface case.

To extend applications of the DIScrete-Ordinate Radiative Transfer (DISORT) code for systems including two media (atmosphere and ocean, atmospthere and ice, etc.), Jin and Stamnes[9] developed a Coupled DISORT (CDISORT). The CDISORT code accounts for change in the refractive index change at the boundary of the two media. For radiative transfer in such a coupled system, CDISORT treats the ocean or ice the same as

1

atmospheric layers but with different optical properties, particularly, different refractive indices. However, the interface between two strata with different refractive indices was considered as flat. This flat surface assumption limits the applications of CDISORT; the afore-mentioned wind-blown ocean surface is hardly flat. In addition to affecting reflection, the surface roughness itself significantly affects the directional character of the beam transmitted beneath the air-water interface. Gjerstad and co-workers[10] proposed an ad hoc method to consider the surface roughness in the discrete-ordinate method. They mimic the irradiances from a Monte Carlo model by adjusting the refractive index in CDISORT . This method has a number of limitations, for example, it calculates irradiances in the ocean only. In this paper, we present a more consistent and widely applicable solution of the discrete ordinate radiative transfer problem in the coupled atmosphere-ocean system with rough surface.

2. Equation and Solution of Radiative Transfer

In order to incorporate the ocean surface roughness into the radiative transfer equation and obtain an analytical solution through the discrete-ordinate method, we need to make the following assumptions:

  ➢ The rough surface can be resolved as a series of small planar facets and, the orientations (slopes) of these facets follow a certain statistical distribution, for example, the Gaussian distribution described by Cox and Munk[1].

  ➢ The dimensions of the elemental facets and surface undulations are large compared with the wavelength of light, so geometric optics can be applied to calculate the reflection and refraction at the surface.

➢ The optical depth of either the ocean or the atmosphere is independent of the surface roughness or horizontal position because statistically, there is no difference between any two points on the surface.

Under these assumptions, the time-averaged radiative effects at any two points on surface are the same, and a patch of surface area at an instant in time in which every possible slope occurs can represent the surface as a whole. Therefore, radiative transfer in a coupled system with horizontally homogeneous atmosphere and ocean and with rough ocean surface is still in the one-dimensional category, as long as the calculated radiation is considered to be time-averaged (statistically averaged) for a point or to be relevant to surface area larger than the patch afore-mentioned for an instant. We also treat the radiance and the reflection and refraction at the ocean surface as scalar. Therefore, the model presented here should not be applied to problems where polarization is important.

Jin and Stamnes[9] (hereafter referred to as JS94) presented in detail the solution for coupled (i.e., air-sea) radiative transfer by the discrete-ordinate method for the flat ocean case. Here we will follow the same conventions defined in JS94 to describe the discrete-ordinate radiative transfer equation and solution for the rough surface case. Because the formulations have a lot in common between these two cases, we will omit most common derivations and emphasize the differences here.

For the flat surface case, the ocean was divided into a totally reflecting angular domain where upwelling photons cannot return directly to the atmosphere, and a refracting

domain where upwelling photons can pass the interface directly to the atmosphere. However, once the surface roughness is introduced, there are no such distinct angular domains. Because of the possible ranges of angles for both the incident photons and the surface interfaces, photons in the atmosphere may pass an interface directed to any angle downward; and vice versa for photons from ocean to atmosphere. This difference results in different radiative transfer solutions.

The radiative transfer equation to be solved for a plane-parallel medium with one dimension can be written as

$$\mu \frac{dI(\tau,\mu,\phi)}{d\tau} = I(\tau,\mu,\phi) - \frac{\omega(\tau)}{4\pi} \int_0^{2\pi} d\phi' \int_{-1}^{1} p(\tau,\mu,\phi,\mu',\phi') I(\tau,\mu',\phi') d\mu' + Q(\tau,\mu,\phi) \quad (1)$$

where $I(\tau,\mu,\phi)$ is the radiance at vertical optical depth τ (measured downward from the upper boundary) and in direction (μ, ϕ); μ is the cosine of the zenith angle (positive for upward directions); ϕ is the azimuth angle; ω is the single scattering albedo; $p(\tau,\mu,\phi,\mu',\phi')$ and $Q(\tau,\mu,\phi)$ are the phase function and source term respectively. We only consider the solar radiation (i.e., not terrestrially emitted thermal infrared or microwave). The solar beam source, $Q(\tau,\mu,\phi)$, is different from the case of a flat ocean. In the flat surface case, part of the downwelling solar beam is reflected specularly back to the atmosphere, and the rest is refracted into the ocean at an angle which depends on the refractive index; this results in two terms (downwelling and reflected) in the solar source function for the atmosphere (Equation 3 in JS94) and one refractive index dependent term for the ocean (Equation 4 in JS94). However, for the case of rough ocean, the solar beam is diffused to various directions when it hits the surface.

4

Therefore, there is no beam source term in the ocean and only one expression in the atmosphere for the rough ocean case, which is

$$Q(\tau,\mu,\phi) = \begin{cases} \omega(\tau)\Big/4\pi \, F_0 p(\tau,\mu,\phi,-\mu_0,\phi_0)\exp(-\tau/\mu_0), & \tau \le \tau_a \\ 0, & \tau > \tau_a \end{cases} \tag{2}$$

where τ_a is the total optical depth of the atmosphere, μ_0 is the cosine of the solar zenith angle, ϕ_0 is the solar azimuth angle, and F_0 is the solar-beam intensity at the top of the atmosphere.

Expanding the radiance $I(\tau,\mu,\phi)$ into a Fourier cosine series of 2N and the phase function $p(\tau,\mu,\phi,\mu',\phi')$ into a series of 2N Legendre polynomials, the discrete-ordinate method converts Equation (1) into a system of azimuthally independent, coupled differential equations for each of the Fourier components. Detailed derivations of these equations were given in JS94 and will not be repeated here. Following the same procedure, the equations for each azimuth radiance component (here we omit the index denoting the order of Fourier series) can be derived, which are in the atmosphere

$$\mu_i^a \frac{dI(\tau,\mu_i^a)}{d\tau} = I(\tau,\mu_i^a) - \sum_{\substack{j=-N_1 \\ j\neq 0}}^{N_1} \omega_j^a D(\tau,\mu_i^a,\mu_j^a)I(\tau,\mu_j^a) + X_0(\tau,\mu_i^a)\exp(-\tau/\mu_0),$$
$$i = \pm 1, \pm 2, \cdots, \pm N_1; \quad \tau \le \tau_a \tag{3a}$$

and in the ocean

$$\mu_i^o \frac{dI(\tau,\mu_i^o)}{d\tau} = I(\tau,\mu_i^o) - \sum_{\substack{j=-N_2 \\ j\neq 0}}^{N_2} \omega_j^o D(\tau,\mu_i^o,\mu_j^o)I(\tau,\mu_j^o),$$
$$i = \pm 1, \pm 2, \cdots, \pm N_2; \quad \tau > \tau_a. \tag{3b}$$

Equations (3a) and (3b) are analogous to the Equations (7) and (8) in JS94, but with different source terms. Here $2N_1$ and $2N_2$ are the numbers of quadrature points (i.e.,

stream numbers) applied in the atmosphere and ocean, respectively. $D(\tau, \mu_i, \mu_j)$ and

$X_0(\tau, \mu_i)$ were also defined in JS94. The (μ_i^a, ω_i^a) and (μ_i^o, ω_i^o) are quadrature points and

weights for the atmosphere and ocean, respectively, with $\mu_{-i} = -\mu_i$ and $\omega_{-i} = \omega_i$. They

have the following relationships:

$$\mu_i^o = \sqrt{1 - [1 - (\mu_i^a)^2]/(\tfrac{n_w}{n_a})^2}, \quad i = 1,2,\cdots,N_1, \qquad (4)$$

$$\omega_i^o = \frac{n_a^2 \mu_i^a}{n_w^2 \mu_i^o} \omega_i^a, \quad i = 1,2,\cdots,N_1. \qquad (5)$$

Here n_a and n_w represent the refractive indices of air and water, respectively. Following

the same procedure as in JS94, the solutions for Equations (3a) and (3b) can be obtained

as

$$I(\tau, \mu_i^a) = \sum_{j=1}^{N_1} \left[C_{-j} G_{-j}(\mu_i^a) \exp(k_j^a \tau) + C_j G_j(\mu_i^a) \exp(-k_j^a \tau) \right] + Z_0(\mu_i^a) \exp(-\tau/\mu_0), \quad (6a)$$
$$i = \pm 1, \pm 2, \cdots, \pm N_1; \quad \tau \leq \tau_a$$

$$I(\tau, \mu_i^o) = \sum_{j=1}^{N_2} \left[C_{-j} G_{-j}(\mu_i^o) \exp(k_j^o \tau) + C_j G_j(\mu_i^o) \exp(-k_j^o \tau) \right], \quad (6b)$$
$$i = \pm 1, \pm 2, \cdots, \pm N_2; \quad \tau > \tau_a.$$

with constants $C_{\pm j}$. k_j and G_j are eigenvalues and eigenvectors, respectively,

determined by solving an algebraic eigenvalue problem as described in Stamnes et al.[11].

$Z_0(\mu_i^a)$ is defined and obtained by solving the Equation (12b) in JS94. The solutions

represented by (6a) and (6b) are seemingly simpler than those in JS94 for the flat ocean

case. However, the solution is not complete yet, because constants $C_{\pm j}$ in (6a) and (6b)

are still unknowns which differ from layer to layer in the atmosphere and the ocean (for

simplicity, we omitted the index denoting layers here). These constants will be

determined by boundary and interface conditions for radiances (intensities).

6

The conditions for the top and bottom boundaries, for the interfaces among atmospheric layers, and for the interfaces among oceanic layers are same as those for the flat ocean case, which were given by Equations (16a), (16b), (16f) and (16g) in JS94. However, the continuity conditions for radiances at the interface between the atmosphere and ocean are very different from those for the flat ocean case. If we denote τ_a^- as the optical depth just above the ocean surface (i.e., the mean sea level) and τ_a^+ as that just below the surface, these conditions for the rough surface case can be expressed as

$$I(\tau_a^-,\mu_i^a) = \sum_{j=1}^{N_1} I(\tau_a^-,-\mu_j^a)R(\mu_i^a,\mu_j^a,n_w/n_a) + \sum_{j=1}^{N_2} I(\tau_a^+,\mu_j^o)T(\mu_i^a,\mu_j^o,n_a/n_w)$$
$$+ \frac{1}{\pi}\mu_0 F_0 \exp(-\tau_a/\mu_0)R(\mu_i^a,\mu_0,n_w/n_a), \qquad (7)$$
$$i = 1,2,...,N_1$$

$$I(\tau_a^+,-\mu_i^o) = \sum_{j=1}^{N_1} I(\tau_a^-,-\mu_j^a)T(\mu_i^o,\mu_j^a,n_w/n_a) + \sum_{j=1}^{N_2} I(\tau_a^+,\mu_j^o)R(\mu_i^o,\mu_j^o,n_a/n_w)$$
$$+ \frac{1}{\pi}\mu_0 F_0 \exp(-\tau_a/\mu_0)T(\mu_i^o,\mu_0,n_w/n_a), \qquad (8)$$
$$i = 1,2,...,N_2$$

in which reflection R and transmission T matrices appear without indices denoting the Fourier order. Equations (7) and (8) show that the emerging radiance at any direction at the air-water interface depends on incidences from all directions from both the atmosphere and ocean for the rough ocean case. This contrasts with the simple one to one correspondence (pairing of each μ_1^a and μ_1^o) as presented by equations (16c-16e) in JS94 for the radiances across the air-water interface of a flat ocean. One asset of the rough ocean case is the term accounting for the diffusion of the solar beam (the last term in (7) and (8)); it makes a simpler formulation of the particular solution (Equations (6a) and

(6b)) than for the flat ocean case in JS94. The reflection and transmission matrices are
calculated as

$$R(\mu,\mu',n) = \frac{2-\delta_{m0}}{2\pi} \int_0^{2\pi} \tilde{R}(\mu,\phi,\mu',\phi',n)\cos m(\phi-\phi')d(\phi-\phi') \qquad (9)$$

$$T(\mu,\mu',n) = \frac{2-\delta_{m0}}{2\pi} \int_0^{2\pi} \tilde{T}(\mu,\phi,\mu',\phi',n)\cos m(\phi-\phi')d(\phi-\phi') \qquad (10)$$

$$\delta_{m0} = \{\begin{array}{ll} 1, & if\ m=0 \\ 0, & otherwise \end{array}$$

Here $\tilde{R}(\mu,\phi,\mu',\phi',n)$ and $\tilde{T}(\mu,\phi,\mu',\phi',n)$ represent the reflection and transmission

functions at the rough surface, respectively (see Appendix A). (μ', ϕ') and (μ, ϕ) are the

incident and exit light directions, respectively. Note that in these functions, n is the

relative refractive index, which equals n_w/n_a if the incident light is from the air (n_a/n_w

if the incidence is from the ocean). The reflectance and transmittance at the rough surface

is closely related to the slope distribution of the surface facets. This distribution is usually

expressed as a Gaussian function as[1]

$$P(\mu_n) = \frac{1}{\pi\sigma^2}\exp(-\frac{1-\mu_n^2}{\sigma^2\mu_n^2}) \qquad (11)$$

Where μ_n is the cosine of the normal to the surface facet. The σ is the mean slope

distribution width and based on Cox and Munk[1], it is related to the wind speed U (m/s) as

$$\sigma^2 = 0.003 + 0.00512U \qquad (12)$$

The shadowing effect and multiple scattering (reflection) among the surface wave facets

are also taken into account in the reflection and transmission functions[12,13]. More details

on these functions ($\tilde{R}(\mu,\phi,\mu',\phi',n)$ and $\tilde{T}(\mu,\phi,\mu',\phi',n)$) are provided in Appendix A.

Substituting (6a) and (6b) into the boundary and interface conditions [i.e., the Equations (16a), (16b), (16f) and (16g) in JS94 and the Equations (7) and (8) here], we obtain a system of linear algebraic equations for the unknown coefficients C_j. The method to solve the equations and obtain the unknown coefficients was described in Stamnes et al.[11] and is not repeated here. The implementation of these solutions into the CDISORT code is not trivial, however.

3. Examples of Model Simulations

3.1. Brief Description of Model

The CDISORT just described has been used as the radiative transfer solver by our Coupled Ocean-Atmosphere Radiative Transfer (COART) model[14-15] (http://www-cave.larc.nasa.gov/cave/).   CDISORT accounts for the change in refractive index at the air-sea interface[9] and now includes the interface roughness into the analytic solution of the radiative transfer equation. Hence COART considers the atmosphere and ocean as one system and treats the ocean strata just as additional "atmospheric" layers with different optical properties. COART models the absorption and scattering processes in atmosphere and ocean explicitly. These include the scattering and absorption by molecules, aerosols and clouds in the atmosphere, and by liquid water molecules, dissolved and particulate matter in the ocean.

COART calculates radiances and irradiances at any level of the atmosphere and ocean in both narrowband (spectral) and broadband. For the narrowband scheme, users can specify both the band (wavelength) limits and computational resolution arbitrarily. In this

scheme, COART employs the LOWTRAN 7 band model (spectral resolution of 20 cm^{-1})

and molecular absorption database for the atmosphere. This corresponds to a wavelength

resolution of about 0.5 nm at 500 nm and 8 nm at 2000 nm. For efficient broadband

calculations of radiance and irradiance, COART divides the solar spectrum (0.20-4.0μm)

into 26 fixed wavelength intervals; in each spectral interval, the k-distribution technique

parameterizes molecular absorption in the atmosphere using the HITRAN 2000

database[16].

The most prominent effects of ocean surface roughness on solar radiation are on

upwelling fields in the atmosphere and downwelling fields in the ocean. Its effects on the

downwelling radiation in the atmosphere and the upwelling radiation in the ocean are

significantly smaller. While COART can simulate a variety of quantities, including the

water-leaving radiance, we show here mainly the types of calculations that pertain to

surface roughness.

3.2. *Effects of Surface Roughness on Radiance*

The COART calculations in Figure 1, which use a McClatchey Midlatitude Summer

atmosphere[17] with marine aerosol optical depth of 0.1 (at 500 nm) and Case 1 water for

ocean[18] with chlorophyll concentration of 0.1mg/m^3, span the upwelling radiance

distribution at the top of atmosphere (TOA) and the downwelling radiance distribution at

four depths in the ocean (0 m, 10 m, 100 m, and 200 m) for three different wind speeds.

The average Petzold[19] phase function for marine particle scattering is used in the

calculations. Figure 1 uses polar coordinates, with view zenith angle (θ) on the radial axis

and relative azimuth angle (ϕ) as the azimuthal coordinate. To facilitate comparisons of different wind speeds, wavelengths and levels, the radiance in Figure 1 is normalized by the upwelling or downwelling irradiance (E) at the same level to obtain the Anisotropic Radiance Function (*ARF*) as

$$ARF(\theta,\phi) = \frac{\pi I(\theta,\phi)}{E} \tag{13}$$

where E is the upwelling irradiance if $I(\theta,\phi)$ is the upwelling radiance (θ is positive in this case in Figure 1) and otherwise, E is the downwelling irradiance (θ is negative in this case). *ARF* here is in fact the ratio of the actual radiance, $I(\theta,\phi)$, and the imagined isotropic radiance, E/π, with the same irradiance. Therefore, the gradient in ARF represents the departure of radiance field from the isotropic case (ARF=1.0).

The solar zenith angle in Figure 1 is 40 degrees. Because the slope distribution in Equation (11) is independent of the wind direction, the ARF (and the radiance field itself) of Figure 1 is symmetric with the principal plane (the vertical plane containing the sun, the surface target and the nadir). So only ARF for azimuth from 0° to 180° is presented. The entire principal plane is covered by the horizontal axis of each panel in Figure 1 and the sun (observer) is on the left (right). The top three rows of Figure 1 show upwelling ARF for the broadband shortwave (0.20-4.0μm), 531 nm (the central wavelength of MODIS channel 11), and 865 nm (MODIS channel 16), respectively. The bottom four rows show downwelling ARF at four ocean depths for 531 nm only (865 nm is not shown because of strong absorption by liquid water and the broadband is not shown because it is similar to 531 nm).

The three columns of Figure 1 cover wind speeds of 3 m/s, 6 m/s, and 10 m/s for atmospheric ARF and wind speeds of 3 m/s, 9 m/s, and 18 m/s for ocean ARF. The hot spot in each panel represents the specular reflection (the sunglint in atmosphere) or transmission (in ocean) of the solar beam at the rough surface. The sunglint is conspicuous at the right of each TOA panel (top 3 rows), but the sunglint region widens as wind speed increases and is much more prominent for the 865 nm case because of less atmospheric scattering. Because the downwelling radiation in the upper ocean is sharply focused around the refracted solar beam, a larger wind variation than for the atmosphere is required to show the hot spot variation with wind (i.e., the widening as wind increasing). As depth in ocean increases, however, the sharp radiance peak around the refracted solar beam rapidly decreases and the position of the maximum radiance gradually shifts from the refracted solar zenith direction to the nadir. At deep ocean levels, the diffusion by ocean water and particles becomes more important and the wind effect on ARF or the radiance anisotropy diminishes. Eventually, the radiance distribution in deep water will approach to an asymptotic shape with maximum at the nadir. The asymptotic distribution is independent on the surface roughness or wind speed but dependent only on the inherent optical properties (IOP) of ocean. However, how quick of the approaching process to the asymptotic distribution depend on both the ocean IOP and the surface roughness. The radiance distribution approaches to the asymptotic shape faster for a high scattering water than for a high absorption water, and faster for a high wind than for a low wind.

For the same atmospheric and ocean inputs, Figure 2 further shows the radiance distribution at 531 nm only; and just around the hot spots in Figure 1 in the principle plane, where radiance varies most sharply and wind effect is most glaring. Figure 2 highlights the different impacts of wind on the radiance fields at various levels in the atmosphere and ocean. Three different wind speeds (3 m/s, 6 m/s and 9 m/s) are used here. Note, the radiance in the sun-glint region at the TOA could be larger than at the surface when wind is weak, because the reflected solar radiances at surface in this particular small region are much larger than the radiances outside; and the Rayleigh and aerosol radiances at TOA are not enough to compensate the attenuation of the strong reflected solar radiance at the surface. While the color scale of row 5 in Figure 1 revealed virtually no effect of surface roughness on downwelling radiance broadly over the hemisphere, rows 2-3 of Figure 2 show that wind indeed has an impact on the radiance distribution around the forward scattering direction in ocean. Figure 2 further delineates how the wind effect diminishes, and the radiance anisotropy rapidly decreases, as depth in ocean increases.

Figure 3 shows a model-observation comparison of the shortwave radiances at the TOA. The measurement data were from NASA's Cloud and Earth Radiation Energy System (CERES) instrument[20] during a special field program at the CERES Ocean Validation Experiment (COVE) site[21]. CERES concerns radiation energy budget over global ocean. The COVE site may not be strictly the case 1 water. However, in *situ* measured ocean optical properties (absorptions for phytoplankton and non-pigment particles, and for CDOM) instead of the parameterization for case 1 water were directly used in the model.

CERES was programmed to a special mode for intense observation at COVE and only the measurements in those clear days during the field experiment are presented here. In this experiment, comprehensive measurements on a variety of physical and optical properties of the atmosphere, surface and ocean were also available for the model input here. The horizontal coordinate in Figure 3 is the sunglint angle, defined as the angle between the view direction and the specular solar reflecting direction for an imagined flat surface. The nine numbers in the lower portion of Figure 3 are the mean model-observation biases for the nine glint-angle intervals (10 degrees each) from 0 to 90, respectively. Though the aerosol loadings and the surface and ocean properties were different for different days, the model and observation agrees fairly well away from the sunglint region. The difference is somewhat larger near the sunglint center (smaller glint angles), probably due to the error in the surface roughness treatment in the calculations, for example, the uncertainties in the Cox-Munk model. The SZA is around 20 degrees when CERES made the measurements, and so a large glint-angle (larger than 75 in Figure 3) also represents a large view zenith angle, where the view path is longer and surface footprint is larger, and therefore the possible horizontal variations of aerosol and surface have larger effects than at a small view angle. This might be responsible for the increased biases in the large angle regime.

3.3. *Effects of Surface Roughness on Irradiance and Albedo*

The effects of ocean surface roughness on irradiances are shown in Figure 4, which has upwelling irradiances in the atmosphere (linear scale) and downwelling irradiances (log

scale) in the ocean for 531 nm, 865 nm and the broadband shortwave (the three columns) at four different levels (the four rows). The model inputs for the atmosphere and ocean are identical in Figures 1 and 4. In each panel of Figure 4, the irradiances for different wind speeds are presented as a function of the cosine of SZA. Results for a flat ocean case (wind = 0 m/s) are plotted as the solid lines in each panel, and thus the difference of irradiances between a rough ocean case (represented by an non-zero wind) and the flat ocean case represents the surface roughness effect quantitatively. Figure 4 shows that the effect of surface roughness is smaller for high sun than for low sun; and the upwelling irradiance just above the surface (row 2) is the field with the most action. Note that for upwelling irradiance at low sun, roughness has a larger effect at 865 nm (where much of the downwelling irradiance is direct, striking the surface at a glancing angle, thereby obtaining strong Fresnel reflection) than at 531 nm (where the downwelling irradiance is more diffuse and has a component that is closer to normal). However, we find the opposite for high sun: roughness has a larger effect on above-surface upwelling irradiance at 531 nm than at 865 nm. The turning point is at approximately SZA of 60 (cosSZA of 0.5), where the direct and diffuse reflectances are similar and this angle can be considered as an "effective" angle for diffuse radiation. For each rough surface case, the variation with respect to the flat surface case (the solid line) in the downwelling irradiance just below the surface (row 3) is equivalent to the variation in the upwelling irradiance just above the surface (row 2) but with opposite sign. However, because the downwelling irradiance just below the surface is much larger than the upwelling irradiance just above the surface, the relative variation in the downwelling irradiance in ocean from the flat ocean case to a rough surface case is smaller and is less obvious than

in the upwelling in atmosphere in Figure 4, especially for high sun conditions. At depth

of 10 m (row 4), the effects of internal ocean optics on irradiance outweigh the effects of

surface roughness and the irradiance at 865 nm is none due to strong water absorption.

Because the downwelling irradiance in the atmosphere has little dependence on the

surface condition of an ice-free ocean, the large effect of surface roughness on upwelling

energy (top half of Figure 4) will have a signal in the surface albedo. The left panel of

Figure 5 shows the MFRSR measured (670 nm) (the dots) and modeled (the solid lines)

surface albedo for three clear afternoons with quite different wind regimes (right panel) at

COVE; the aerosol loadings were low. Aerosol optical properties used in model were

measured from the same platform by NASA's Aeronet Cimel instrument[22]. The Cimel

sun photometer made periodic scans in the almacantur and in the solar principal plane;

inversions of these data yielded aerosol phase functions and particle size distributions[23].

The wind data were from the NOAA meteorology station also at COVE. The ocean

optical properties and chlorophyll concentration were also from in situ measurements[15],

but ocean optics has little effect on the total surface albedo at 670 nm. To remove the

relative difference between the two surface-based MFRSR instruments and obtain

accurate ocean albedos, the instruments subsequently used for the downwelling and

upwelling spectral irradiance measurements were calibrated relative to each other in

advance, by observing the same target at the same time[15,21]. Results in Figure 5 show the

significant effects of wind on ocean surface albedo, especially for large SZA. The

dependences of albedos on SZA and wind are consistent between model and

measurements.

When light is incident on the rough surface at a grazing direction, the photons are more likely to undergo multiple scattering or reflection among the surface wave facets. There is also a shadowing effect of one wave facet blocking rays from getting to another facet (occultation)[13]. Figure 6 shows the effects of multiple reflection and shadowing among the surface wave facets on albedo simulation. In each panel, the solid line is the modeled albedo same as shown in Figure 5, with both shadowing and multi-reflection considered. The short dashed line is the calculation without shadowing but with multi-reflection, while the long dashed line represents the results without any multi-reflection but with shadowing considered. The dotted line is the calculation without roughness (flat surface). The error bar shows the range of measured albedo within 3 degrees of SZA centered by the error bar. As expected, the calculated albedo is reduced after including the shadowing effect and is increased after including the multi-reflections. The effect of multi-reflection is larger on day 1 when the wind was high and the model-observation agreement is improved after the effects of shadowing and multi-reflection are taken into account. However, the effects of shadowing and multi-reflection are small for high sun (small SZA). The small differences between the flat ocean albedos (the dotted lines) are mainly due to the slightly different aerosol loadings for the three selected days.

Results above show that the surface roughness has largest effect on ocean albedo at low sun (large SZA). Both Figure 5 and Figure 6 show a larger model-observation discrepancy for large SZA (higher than about 80) for the day with strongest wind (day 1). This may indicate a larger error tendency in the Cox-Munk surface roughness model in

high wind conditions. An alternate distribution was recently produced by Ebuchi and Kizu[24], based on approximately 30 million satellite observations over five years. The Ebuchi-Kizu function has a narrower slope distribution, and less sensitivity to wind, than the Cox-Munk function. The calculated albedo (not shown) based on the Ebuchi-Kizu model is close to that based on the Cox-Munk model for low winds, but higher for high wind and large SZA. However, we cannot conclude the superiority of either the surface roughness parameterization, based on limited comparison. Validation of this parameterization is not a subject here. We simply indicate that the surface slope distribution function has significant impact on the albedo calculation too. On the other hand, the radiative transfer model itself could also introduce errors for calculations with large SZA. For example, we have not accounted for the orientation of wave slope with wind direction and the Earth curvature, both have larger impacts on glancing incidences.

4. Conclusion

We present an analytical approach for radiative transfer in a coupled atmosphere-ocean system having a rough surface between two media with differing indices of refraction. The discrete-ordinate technique is used in the formulation and solution. The solution is implemented in the radiative transfer code – CDISORT. Using CDISORT as the radiative transfer solver, a coupled ocean-atmosphere radiative transfer (COART) model is now available to calculate various radiances and irradiances at any altitude in the atmosphere and depth in the ocean. This model is demonstrated online at http://www-cave.larc.nasa.gov/cave/ (searching "COART model" on Google).

Model simulations show that the ocean surface roughness has significant effects on the upwelling radiation in the atmosphere and the downwelling radiation in the ocean. As wind speed increases, the angular domain of sunglint broadens, the surface albedo under low sun decreases, and transmission through the air-water interface to the interior of the ocean increases. The transmitted radiance just below the ocean surface is highly anisotropic, but this anisotropy decreases rapidly as surface wind increases. Deeper below the surface, as the optical properties of the ocean interior eventually overcome the impact of surface roughness, the anisotropy decreases and the radiance distribution gradually approaches to an asymptotic shape with maximum at the nadir. The effects of surface roughness on radiation depend greatly on both wavelength and angle of incidence (i.e., solar elevation); these effects are significantly smaller throughout the spectrum at high sun.

The models and observations agree fairly well on the effects of surface roughness. Some discrepancies may indicate that the original Cox-Munk surface roughness model is not sufficient for high wind conditions or other errors exist in the treatment of the surface roughness.

Appendix A: Reflection and Transmission at Rough Ocean Surface

The light incident at a flat water surface will be reflected or refracted directly. However, photons incident at the rough surface may scatter more than once among the surface wave facets before exit to air or water. The single scattering reflectance at the air-water interface from (μ', ϕ') to (μ, ϕ) can be written as

$$R_0(\mu,\phi,\mu',\phi',n) = r(\cos\alpha_r,n)\,p(\mu',\phi' \to \mu,\phi,\mu_n^r,\sigma)\,s(\mu,\mu',\sigma) \qquad (14)$$

where $r(\cos\alpha_r,n)$ is the Fresnel reflection coefficient for relative refractive index n under incident angle α_r. $n = n_w/n_a$ for air incidence and $n = n_a/n_w$ for water incidence. The $p(\mu',\phi' \to \mu,\phi,\mu_n^r,\sigma)$ is the fraction of the sea surface (i.e., the effective area of the wave facets) with normal μ_n^r to reflect light from (μ', ϕ') to (μ, ϕ) and is given by

$$p(\mu',\phi' \to \mu,\phi,\mu_n^r,\sigma) = \frac{1}{4\mu(\mu_n^r)^4}P(\mu_n^r) \qquad (15)$$

where $P(\mu_n^r)$ is the surface slope distribution function given by Equation (11). The required surface normal, μ_n^r, to fulfill the specular reflection from (μ', ϕ') to (μ, ϕ) is determined by μ', ϕ', μ, and ϕ. Defining

$$\cos\alpha = \mu\mu' + \sqrt{1-\mu^2}\,\sqrt{1-\mu'^2}\,\cos(\phi-\phi') \qquad (16)$$

$\cos\alpha_r$ in Equation (14) can be derived as

$$\cos\alpha_r = \sqrt{(1-\cos\alpha)/2} \qquad (17)$$

and μ_n^r can be derived as

$$\mu_n^r = \frac{\mu+\mu'}{\sqrt{2(1-\cos\alpha)}} \qquad (18)$$

In Equation (14), the shadowing effect, representing the probability that the incident and the reflected lights are intercepted by other surface waves, is corrected by the function, $s(\mu,\mu',\sigma)$, which is based on Sancer[13] and is widely used[5,7].

Similarly, the single scattering transmittance at the air-water interface from (μ′, φ′) to (μ, φ) can be written as

$$T_0(\mu,\phi,\mu',\phi',n) = r(\cos\alpha_t,n)\,p(\mu',\phi' \to \mu,\phi,\mu_n^t,\sigma)s(\mu,\mu',\sigma) \qquad (19)$$

Where $r(\cos\alpha_t,n)$ is the Fresnel transmission for relative refractive index n for incident angle α_t. $p(\mu',\phi' \to \mu,\phi,\mu_n^t,\sigma)$ is the fraction of the sea surface with the required orientation to refract light from (μ′, φ′) to (μ, φ) and is given by

$$p(\mu',\phi' \to \mu,\phi,\mu_n^t,\sigma) = \frac{n\sqrt{n^2 + \cos^2\alpha_t - 1}}{4\mu(\mu_n^t)^4 \cos\alpha_t} P(\mu_n^t) \qquad (20)$$

The surface normal (μ_n^t) and the incident angle (α_t) required to fulfill the refraction are

$$\cos\alpha_t = \frac{|n\cos\alpha - 1|}{\sqrt{n^2 - 2n\cos\alpha + 1}} \qquad (21)$$

and

$$\mu_n^t = \mu'\cos\alpha_t + \sin\alpha_t\sqrt{1-\mu'^2}\sqrt{1-(1-\mu^2)\sin^2(\phi-\phi')/\sin^2\alpha} \qquad (22)$$

Due to the roughness nature, some photons after a first scattering at the surface may not exit to the air or water directly but experience a second or even higher orders of scattering processes. The reflectance and transmittance from these multiple scattering can be derived from the single scattering values (i.e., R_0 and T_0 represented by Equations 14 and

19) and the slope distribution function. For example, the second scattering reflectance from (μ', ϕ') to (μ, ϕ) is

$$R_1(\mu,\phi,\mu',\phi',n) = \int_{-1}^{1}d\mu_1 \int_{0}^{2\pi}d(\phi_1 - \phi')R_0(\mu_1,\phi_1,\mu',\phi',n)R_0(\mu,\phi,\mu_1,\phi_1,n) \qquad (23)$$

the third scattering reflectance is

$$R_2(\mu,\phi,\mu',\phi',n) = \int_{-1}^{1}d\mu_2 \int_{0}^{2\pi}d(\phi_2 - \phi')R_1(\mu_2,\phi_2,\mu',\phi',n)R_0(\mu,\phi,\mu_2,\phi_2,n) \qquad (24)$$

the fourth scattering reflectance is

$$R_3(\mu,\phi,\mu',\phi',n) = \int_{-1}^{1}d\mu_3 \int_{0}^{2\pi}d(\phi_3 - \phi')R_2(\mu_3,\phi_3,\mu',\phi',n)R_0(\mu,\phi,\mu_3,\phi_3,n) \qquad (25)$$

and so on for higher orders of scattering reflectance. Finally, the total reflectance is

$$\tilde{R}(\mu,\phi,\mu',\phi',n) = \sum_{i=0}^{N} R_i(\mu,\phi,\mu',\phi',n) \qquad (26)$$

This is the reflection function used in Equation (9). Here $N+1$ represents the highest order of multiple scattering to be considered. $N=0$ is for single scattering only. In theory, N could be very large. But large N means more computation time. In reality, most photons will be either reflected or refracted into air or water after a single interaction with the surface. Photons could survive for higher orders of successive multiple scattering decreases rapidly as the scattering order increases. Test results indicate that including the second scattering ($N=1$) is sufficient for virtually all conditions.

Similar to the reflectance, the formulations for multiple scattering transmittance can be written as

$$T_1(\mu,\phi,\mu',\phi',n) = \int_{-1}^{1}d\mu_1 \int_{0}^{2\pi}d(\phi_1 - \phi')R_0(\mu_1,\phi_1,\mu',\phi',n)T_0(\mu,\phi,\mu_1,\phi_1,n) \qquad (27)$$

$$T_2(\mu,\phi,\mu',\phi',n) = \oint_{-1} d\mu_2 \oint_0^{2\pi} d(\phi_2 - \phi') R_1(\mu_2,\phi_2,\mu',\phi',n) T_0(\mu,\phi,\mu_2,\phi_2,n) \qquad (28)$$

$$T_3(\mu,\phi,\mu',\phi',n) = \oint_{-1} d\mu_3 \oint_0^{2\pi} d(\phi_3 - \phi') R_2(\mu_3,\phi_3,\mu',\phi',n) T_0(\mu,\phi,\mu_3,\phi_3,n) \qquad (29)$$

and then the total transmission used in Equation (10) is

$$\tilde{T}(\mu,\phi,\mu',\phi',n) = \sum_{i=0}^{N} T_i(\mu,\phi,\mu',\phi',n) \qquad (30)$$

The effects of multiple scattering on the total reflectance for a beam incidence (direct albedo) and for a diffuse incidence (diffuse albedo) are presented in Figure 7. Albedo represents the irradiance reflectance. The direct albedo for a beam incidence from (μ_0, ϕ_0) is

$$RR(\mu_0) = \frac{1}{\mu_0} \int_0^1 d\mu \int_0^{2\pi} d(\phi - \phi_0) \mu \tilde{R}(\mu,\phi,\mu_0,\phi_0,n) \qquad (31)$$

From the direct albedo, the diffuse albedo can be obtained by integrating *RR* weighted by the incident radiances. For the uniform (isotropic) incidence, this diffuse albedo is simply

$$R_{df} = 2 \oint \mu RR(\mu) d\mu \qquad (32)$$

In Figure 7, the upper two panels are for the direct albedo and the lower two panels are for the diffuse albedo. The left panels are for light incident from air ($n=1.34$) and the right panels are for light incident from water ($n=1/1.34$). Here the water refractive index of 1.34 is used, which is a typical number for visible wavelengths. The solid lines in Figure 7 are for single scattering and the dashed lines are for multiple scattering. In panels (a) and (b), the numbers by each pair of lines on the right edge represent the incident angles.

These results show that the multiple scattering effect is small for radiation with small incident angles and increases as wind speed increases. Note, for a flat surface, the direct albedo is 1.0 (i.e., total reflection) for water-incident light with incident angle larger than the critical angle (which is 48.2^o for n_w=1.34). Figure 7 (Panel b) indicates that this total reflection region disappears when the surface is roughed.

The total transmittance for a beam incidence or for a diffuse incidence simply equals to one minus the total relevant albedo as defined in Equations (31) and (32). Therefore, opposite to the albedo, the multiple scattering will decrease the transmittance across the air-water interface incident from either direction.

Reference

1. C. Cox, and W. Munk, "Measurement of the roughness of the sea surface from photographs of the sun s glitter," J. Opt. Soc. Am., 44, 838-850 (1954).

2. A. Morel and B. Gentili, "Diffuse reflectance of oceanic waters. II: Bidirectional aspects," Appl. Opt., 32, 6,864-6,879 (1993).

3. G.N. Plass, and G.W. Kattawar, "Radiative transfer in the earth's atmosphere and ocean: influence of ocean waves," Appl. Opt., 14, 1924-1936 (1975).

4. J.T.O. Kirk, "The upwelling light stream in natural waters," Limnol. Oceanogr. 34, 1410-1425 (1989).

5. H. Gordon, and M. Wang, "Surface-roughness considerations for atmospheric correction of ocean color sensors. I. The Rayleigh-scattering component," Appl. Opt., 31, 4,247-4,260 (1992).

6. R. W. Preisendorfer and C. D. Mobley, "Albedos and glitter patterns of a wind-roughened sea surface," J. Phys. Oceanogr. 16, 1293-1316 (1986).

7. T. Nakajima, and M. Tanaka, "Effect of wind-generated waves on the transfer of solar radiation in the atmosphere-ocean system," J. Quant. Spectrosc. Radiat. Transfer, 29, 521-537 (1983).

8. J.L., Deuze, M. Herman, and R. Santer, " Fourier series expansion of the transfer equation in the atmosphere-ocean system," J. Quant. Spectrosc. Radiat. Transfer, 41, 483-494 (1989).

9. Z. Jin, and K. Stamnes, "Radiative transfer in nonuniformly refracting layered media: Atmosphere-ocean system," Appl. Opt. 33, 431-442 (1994).

10. K. I. Gjerstad, J. Stamnes, B. Hamre, J.K. Lotsberg, B. Yan, and K. Stamnes, "Monte Carlo and discrete-ordinate simulations of irradiances in the coupled atmosphere-ocean system," Appl. Opt. 42, 2609-2622 (2003).

11. K. Stamnes, S. C. Tsay, W. J. Wiscombe and K. Jayaweera, "Numerically stable algorithm for discrete-ordinate-method radiative transfer in multiple scattering and emitting layered media," Appl. Opt., 27, 2502-2509 (1998).

12. L. Tsang, J.A. Kong, and R.T. Shin, *Theory of Remote Sensing* (Wiley, New York 1985).

13. M. I. Sancer, "Shadow-corrected electromagnetic scattering from a randomly-rough ocean surface," IEEE Trans. Antennas Propag. 17, 557 585 (1969).

14. Z. Jin, T.P. Charlock, K. Rutledge, "Analysis of Broadband Solar Radiation and Albedo Over the Ocean Surface at COVE," J. Atmos. Oceanic Technol., 19, 1585-1601 (2002).

15. Z. Jin, T.P. Charlock, K. Rutledge, G. Cota, R. Kahn, J. Redemann T. Zhang, D.A. Rutan, and F. Rose, "Radiative Transfer Modeling for the CLAMS Experiment," J. Atmos. Sci., 62, 1052-1070 (2005).

16. S. Kato, T. P. Ackerman, J. H. Mather, and E. E. Clothiaux, "The K-distribution method and correlated-k approximation for a shortwave radiative transfer Model," J. Quant. Spectros. Radiat. Trans., 62, 109-121 (1999).

17. R. A. McClatchey, R.W. Fenn, J. E. A. Selby, F. E. Volz, and J. S. Garing, "Optical properties of the atmosphere," AFCRL report AFCRL-72-0497. Air Force Cambridgeh Laboratories, Bedford, MA (1972).

18. A. Morel and S. Maritorena, "Bio-optical properties of oceanic waters: a reappraisal," J. Geophys. Res., 106(C4), 7163-7180 (2001).

19. T.J. Petzold, *Volume scattering functions for selected ocean waters,* (Scripps Institution of Oceanography, 1977).

20. B.A. Wielicki, B. R. Barkstrom, E. F. Harrison, R. B. Lee, G. L. Smith, and J. E. Cooper, "Clouds and the Earth s Radiant Energy System (CERES): An Earth observing system experiment," Bull. Amer. Meteor. Soc., 77, 853-868 (1996).

21. W. L. Smith Jr., T. P. Charlock, R. Kahn, J. V. Martins, L. A. Remer, P. V. Hobbs, J. Redemann, and C. K. Rutledge, "EOS TERRA aerosol and radiative flux validation: An overview of the Chesapeake Lighthouse and Aircraft Measurements for Satellites (CLAMS) experiment," J. Atmos. Sci., 62, 903-918 (2005).

22. B.N. Holben, T.F. Eck, I. Slutsker, D. Tanre, J.P. Buis, A. Setzer, E. Vermote, J.A. Reagan, Y.J. Kaufman, T. Nakajima, F. Lavenu, I. Jankowiak, and A. Smirnov, "AERONET-A federated instrument network and data archive for aerosol characterization," Remote Sens. Environ., 66, 1-16 (1998).

23. O. Dubovik, and M. D. King, "A flexible inversion algorithm for retrieval of aerosol optical properties from sun and sky radiance measurements," J. Geophys. Res., 105, 20673-20696 (2000).

24. N. Ebuchi and S. Kizu, "Probability distribution of surface slope derived using sun glitter images from geostationary meteorological satellite and surface vector winds from scatterometers," J. Oceanogr. 58, 477-486 (2002).
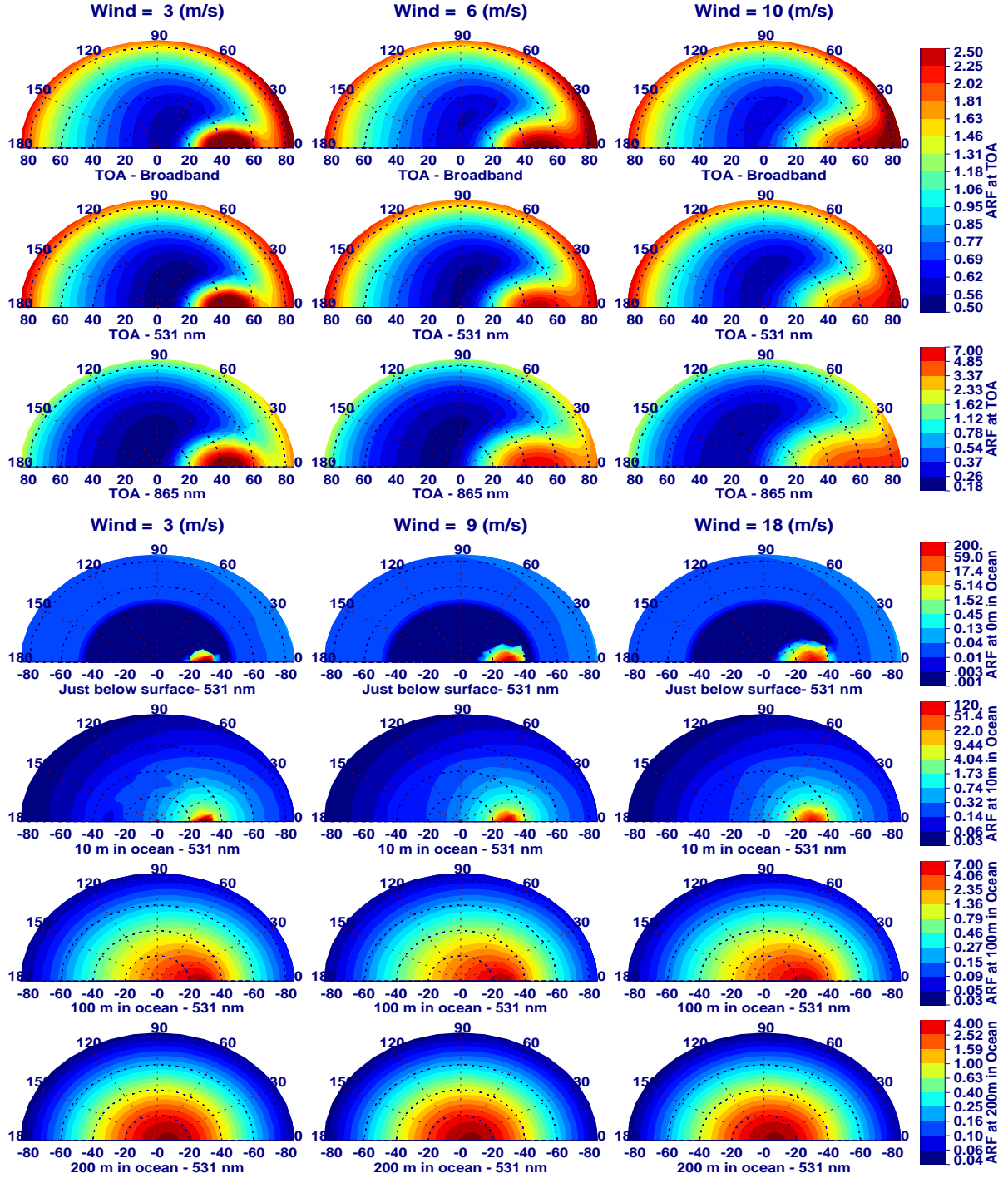
Figure caption:

Figure 1. Model simulated upwelling radiance field at the top of atmosphere (TOA) and
the downwelling radiance field at depths of 0 m, 10 m, 100m and 200 m in the ocean
for three different wind speeds and for three wavelength sets (broadband, narrowband
at 531 nm, and narrowband at 865 nm). The SZA is 40 degrees.

Figure 2. Effects of surface roughness on radiance distributions at 531 nm in the
components of the principal plane containing most of the reflected solar beam in the
atmosphere (top row), and most of the refracted solar beam in the ocean (rows 2-4).
The SZA is 40 degrees.

Figure 3. Comparison of modeled and measured broadband radiances as a function of
sun-glint angle. The nine numbers are the mean model-observation biases for the nine
glint-angle intervals (10 degrees each) from 0 to 90, respectively.

Figure 4. Modeled irradiances versus cos(SZA) with upwelling irradiance in the
atmosphere and downwelling irradiance in the ocean, for different wind speeds and
different wavelengths.

Figure 5. Effects of wind speed on ocean surface albedo at 670 nm. The left panel shows
the modeled and measured surface albedo during three afternoons. The right panel
shows the observed wind speed for each afternoon. Different colors are for different
days.

Figure 6. Effects of multiple scattering (reflection) and shadowing among surface wave
facets on ocean albedo simulation. The three panels are for the three selected days as
in Figure 5. The long dashed line is the albedo computed without multi-reflection but
with shadowing; the short dashed line is the albedo computed without shadowing but

with multi-reflection; the dotted line is the albedo calculated with a flat surface. The error bar represents the measured albedo range within the 3 degrees of SZA.

Figure 7. Effect of multiple scattering on albedo. The upper two panels show the direct albedo (beam incidence) and the lower two panels show the diffuse albedo (isotropic incidence). The left panels are for incidence from air and the right panels are for incidence from water. The numbers by each pair of lines on the right of panels (a) and (b) represent the incident angles in degree. For each pair of lines, the solid line is for single scattering and the dashed one is for multiple scattering.

Figure 1. Model simulated upwelling radiance field at the top of atmosphere (TOA) and the downwelling radiance field at depths of 0 m, 10 m, 100m and 200 m in the ocean for three different wind speeds and for three wavelength sets (broadband, narrowband at 531 nm, and narrowband at 865 nm). The SZA is 40 degrees.
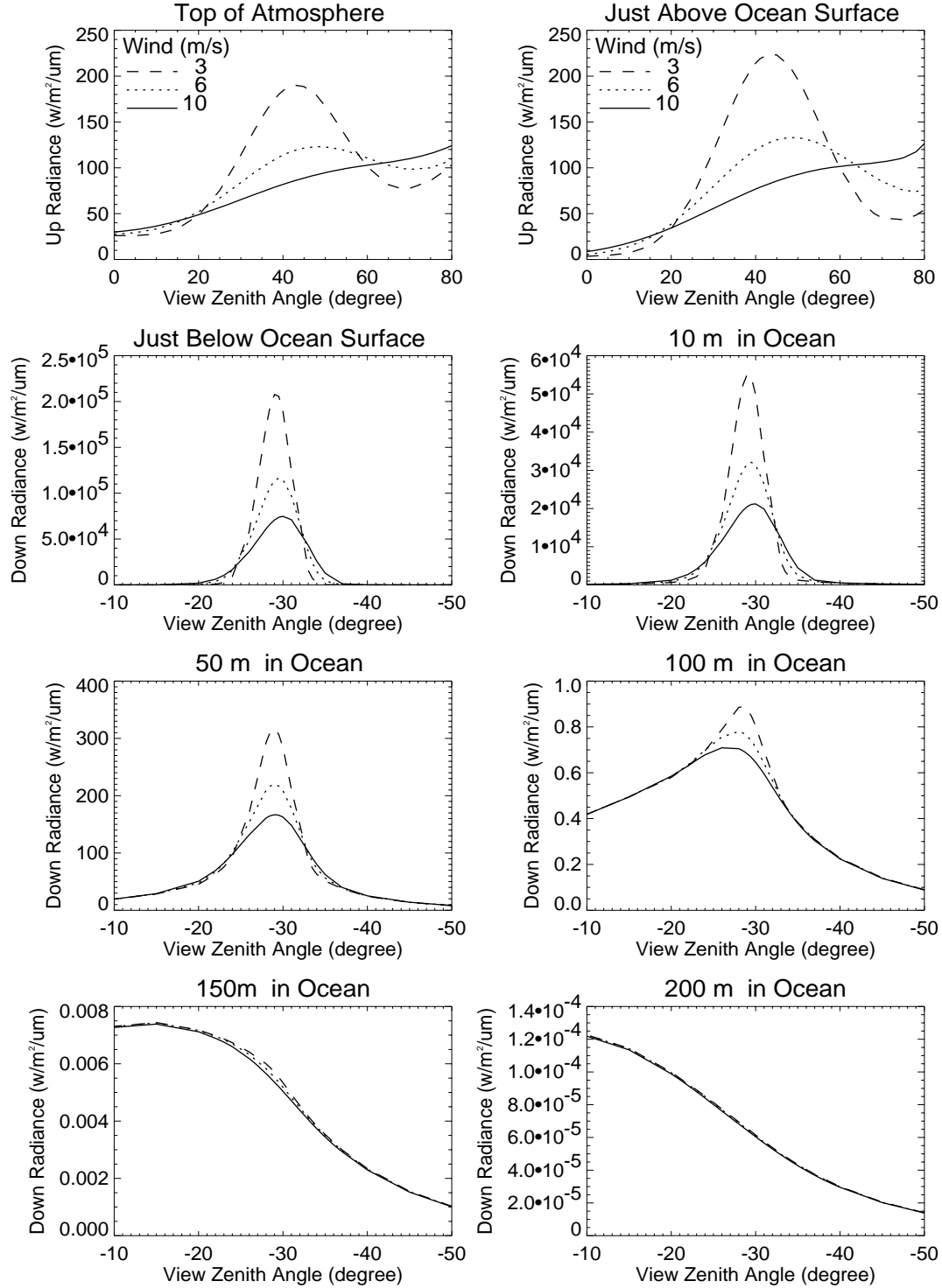
Figure 2. Effects of surface roughness on radiance distributions at 531 nm in the components of the principal plane containing most of the reflected solar beam in the atmosphere (top row), and most of the refracted solar beam in the ocean (rows 2-4). The SZA is 40 degrees.

Figure 3. Comparison of modeled and measured broadband radiances as a function of sun-glint angle. The nine numbers are the mean model-observation biases for the nine glint-angle intervals (10 degrees each) from 0 to 90, respectively.
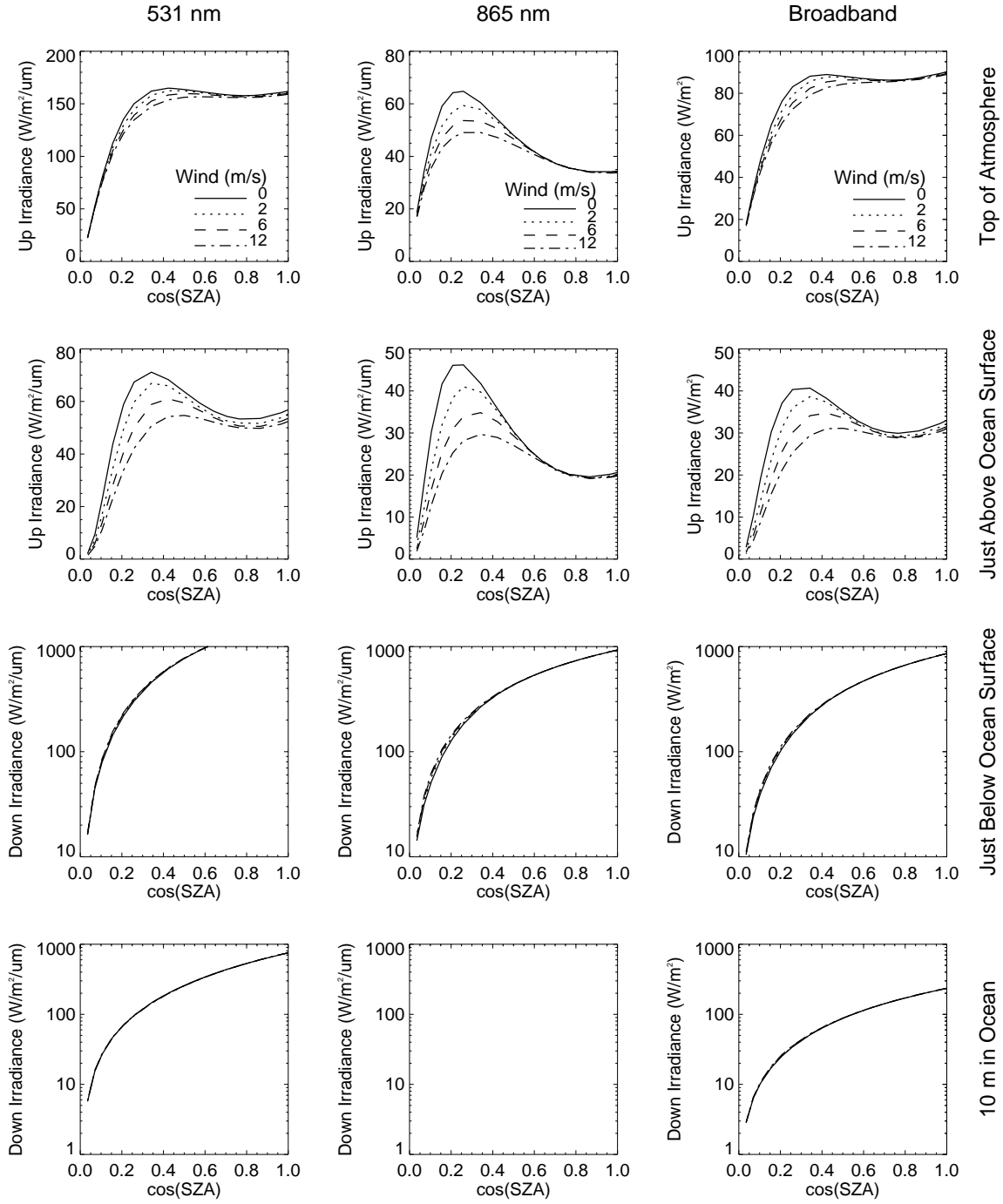
Figure 4. Modeled irradiances versus cos(SZA) with upwelling irradiance in the atmosphere and downwelling irradiance in the ocean, for different wind speeds and different wavelengths.
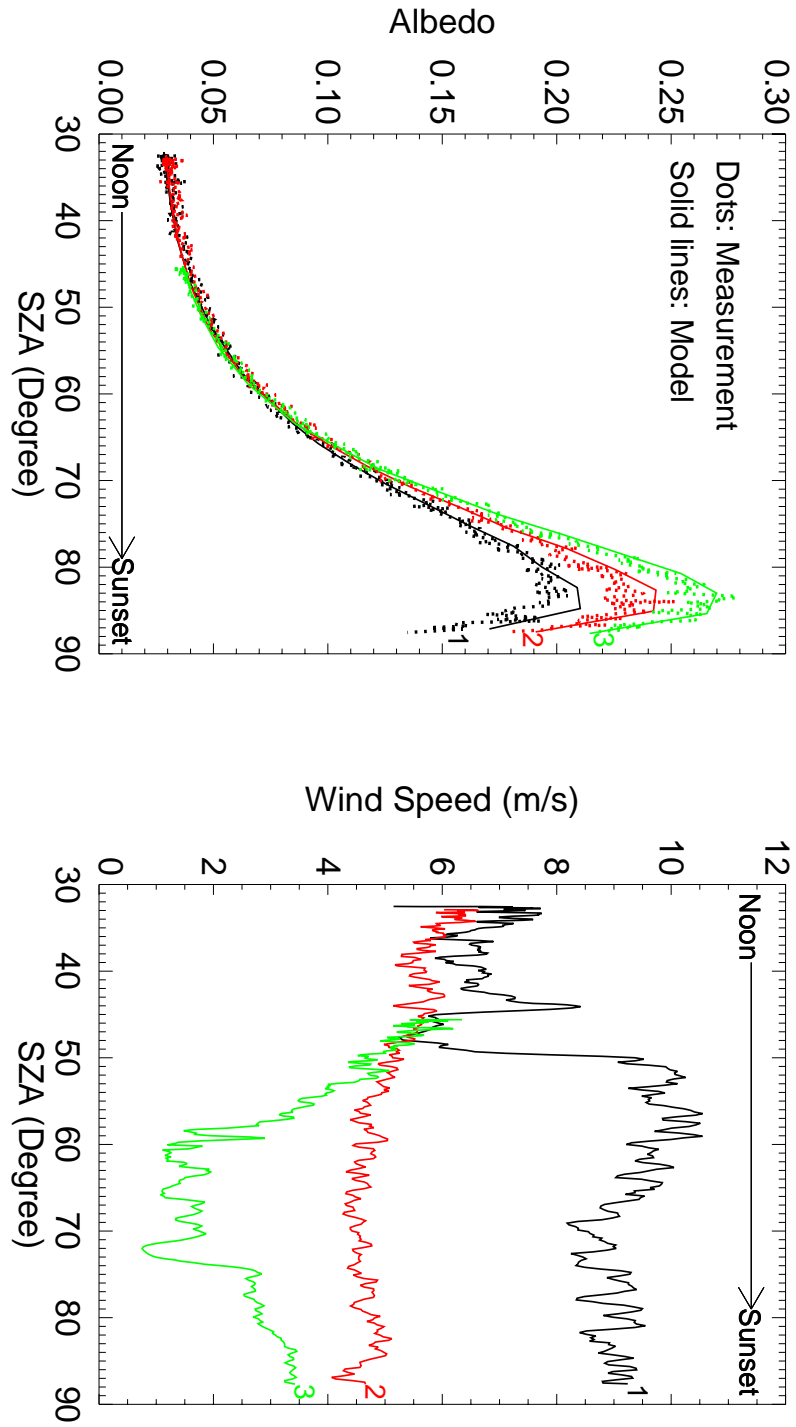
Figure 5. Effects of wind speed on ocean surface albedo at 670 nm. The left panel shows the modeled and measured surface albedo during three afternoons. The right panel shows the observed wind speed for each afterenoon. Different colors are for different days.
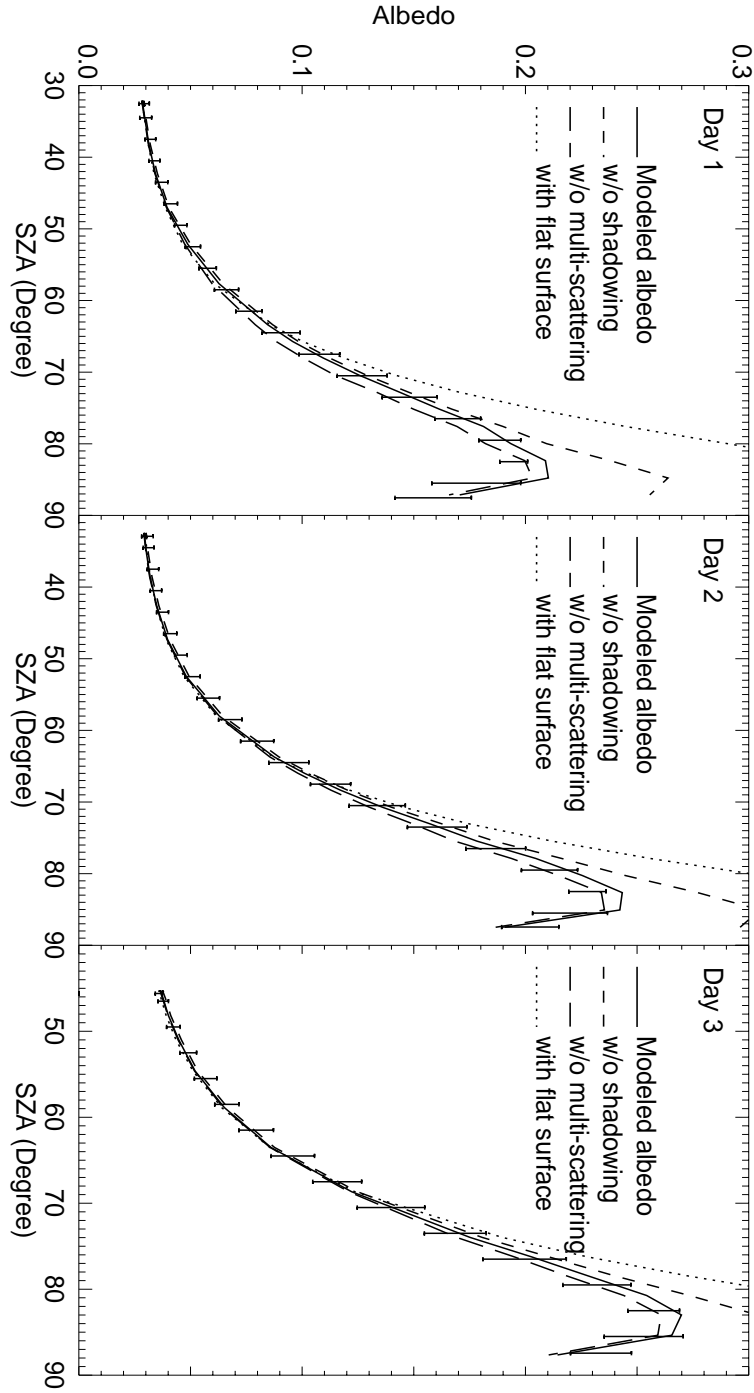
Figure 6. Effects of multiple reflection and shadowing among surface wave facets on ocean albedo simulation. The three panels are for the three selected days as in Figure 5. The long dashed line is the albedo computed without multi-reflection but with shadowing; the short dashed line is the albedo computed without shadowing but with multi-reflection; the dotted line is the albedo calculated with a flat surface. The error bar represents the measured albedo range within the 3 degrees of SZA.
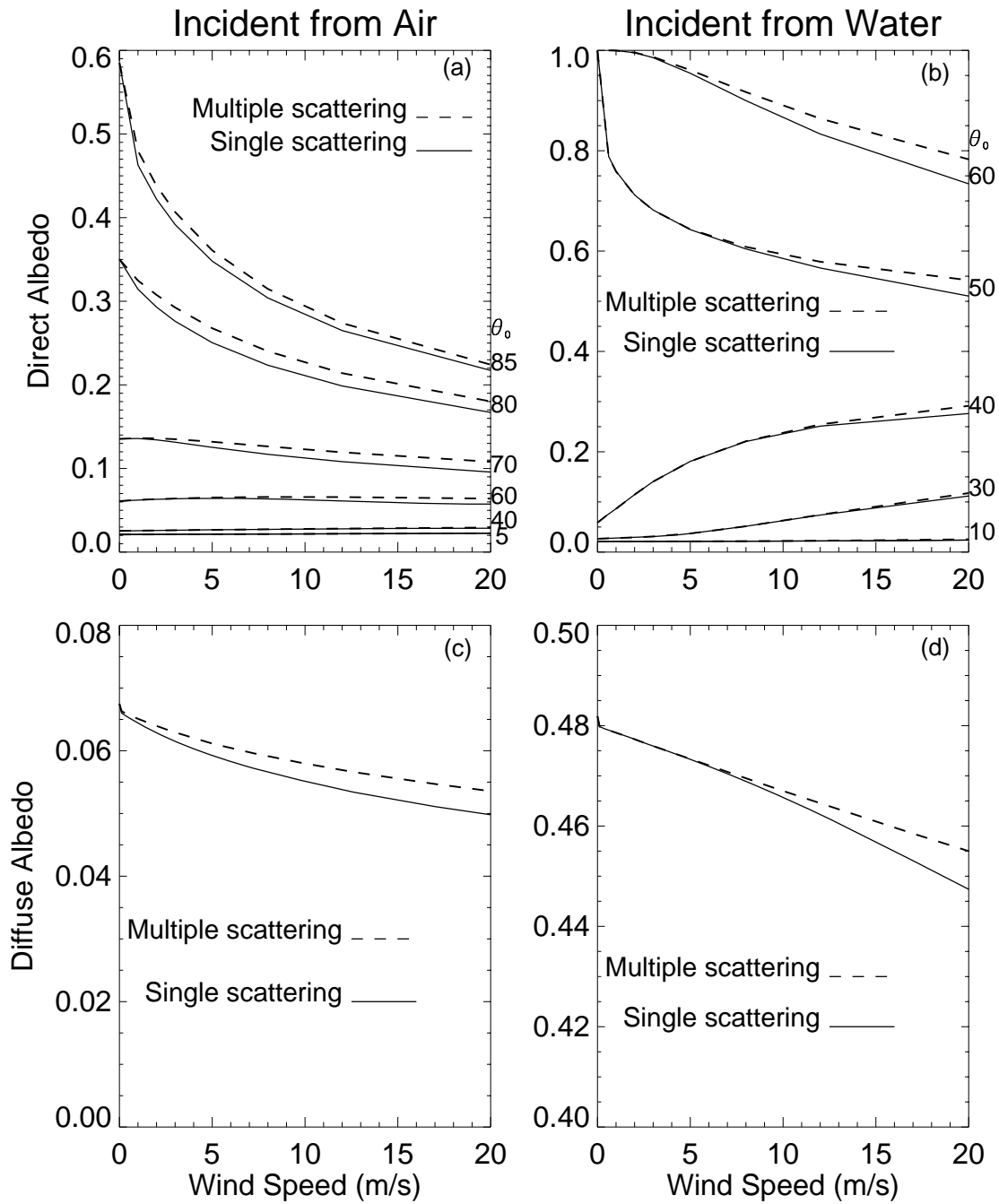
Figure 7. Effect of multiple scattering on albedo. The upper two panels show the direct albedo (beam incidence) and the lower two panels show the diffuse albedo (isotropic incidence). The left panels are for incidence from air and the right panels are for incidence from water. The numbers by each pair of lines on the right of panels (a) and (b) represent the incident angles in degree. For each pair of lines, the solid line is for single scattering and the dashed one is for multiple scattering.